Magnetic Resonance Imaging 58 (2019) 162–173

Contents lists available at ScienceDirect

Magnetic Resonance Imaging

journal homepage: www.elsevier.com/locate/mri

Original contribution

Design and testing of a 24-channel head coil for MR imaging at 3 T

Ye Li[a,b,1], Jo Lee[a,b,1], Lei Zhang[a,b], Qiaoyan Chen[a,b], Changjun Tie[a,b], Chao Luo[a,b], Xiaoliang Zhang[c,d], Dong Liang[a,b], Xin Liu[a,b], Hairong Zheng[a,b,*]

[a] Lauterbur Imaging Research Center, Shenzhen Institutes of Advanced Technology, Chinese Academy of Sciences, Shenzhen 518055, China
[b] Shenzhen Key Laboratory for MRI, Shenzhen 518055, China
[c] Department of Radiology and Biomedical Imaging, University of California San Francisco, San Francisco, CA 94158, USA
[d] UCSF/UC Berkeley Joint Graduate Group in Bioengineering, San Francisco, CA 94158, USA

ARTICLE INFO

Keywords:
Magnetic resonance imaging
RF coil
Phased array
Head coil
Intracranial vessel wall

ABSTRACT

Purpose: To offer the new head coil option (with a lower channel count) of an RF coil array that provides comparable performance to the commercial 32-channel head coil.
Methods: The coil system comprised an upper shield (ten channels) and bottom section (fourteen channels). Signal-to-noise ratio (SNR) values for 2D unaccelerated imaging and the g-factor with an acceleration factor of 2–4 were evaluated in a phantom study. SNR performance and human brain and intracranial vessel wall imaging were conducted as part of the *in vivo* study. Both studies were conducted using the commercial head coil on the Siemens Tim Trio 3 T system for comparison.
Results: In the phantom study, the new head coil had an 8% higher SNR than the commercial head coil and demonstrated less than a 1% difference in the g-factor with the acceleration factor 2–4 in the right-to-left and anterior-to-posterior directions. In the *in vivo* study, the performance matched the results seen in the phantom study and showed high reproducibility in several human experiments. Structural images of the brain and intracranial vessel wall with an isotropic spatial resolution of 0.5 mm can be acquired with the new head coil.
Conclusion: This study demonstrates that the new head coil is capable of providing good SNR performance in both phantom and human experiments, can achieve similar acceleration ability compared to the commercial head coil, and is capable of obtaining brain and intracranial vessel wall images.

1. Introduction

High field (3 T and above) magnetic resonance imaging (MRI) technology is widely applied in intracranial disease diagnosis (*e.g.*, intracranial atherosclerosis) for its high tissue contrast and noninvasive characteristics [1–6]. Therefore, the development of head RF coil arrays used for signal detection which allow for improvement in image quality, has become very important.

To satisfy the resolution requirements of certain applications, the surface array has become known for providing good SNR images and can widen the coverage area and improve the sensitivity of MRI [7–10]. In general, a higher channel count for an RF coil array provides greater sensitivity and spatial image resolution, as well as better parallel imaging performance [11–17]. However, a higher channel count for the RF coil array also increases the challenges of decoupling [7], which will directly lead to attenuation of the SNR [18]. This introduces technical challenges in the design of high-field RF coil arrays, particularly large channel-count arrays, such as those that achieve sufficient electromagnetic decoupling among the resonant elements of the RF array and obtain the appropriate coil size and layout in specific applications [19–27]. The connection between the SNR and the RF coil array count was confirmed as being non-linear and will vary with the distance to the center of the object [18]. For the center image, the SNR changes slowly in the setting of an increase in channel count in the RF array [9,22].

In this study, we investigated a close fitting, newly-designed 24-channel head coil array for the intracranial vessel wall. The device was compared with the Siemens commercial 32-channel head coil array to evaluate its performance in both phantom and *in vivo* studies. We attempted to demonstrate the capabilities of the coil through noise correlation matrixes, SNR maps, inverse g-factor maps, and 3D structural images of the internal carotid artery (ICA), middle cerebral arteries (MCA), and basilar artery (BA).

* Corresponding author at: Room A211, 1068 Xueyuan Blvd, University Town of Shenzhen, Nanshan, Xili, Shenzhen, China.
E-mail address: hr.zheng@siat.ac.cn (H. Zheng).
[1] These authors contributed equally to this work.

https://doi.org/10.1016/j.mri.2019.01.020
Received 30 August 2018; Received in revised form 7 December 2018; Accepted 22 January 2019

2. Methods

2.1. Coil building

To build the shell of the head coil, two requirements were considered: the peripheral edges needed to fit in the notch from the bed of the MRI system, and the inner edge was made to fit close to each subject's head. The shell comprised two parts: the upper shell for covering the human face and the bottom case for resting upon comfortably. The upper shell was further divided into two parts: a top cover and a base. The coil elements rested directly on the base, and the top cover protected the coils from colliding. The bottom case was divided into three parts: a top cover, a base, and a smooth thin shell located in between the two parts. There were some narrow gaps in the base design of the bottom case which made coil wiring difficult. The coil elements distributed in the bottom case were designed to be laid upon the top of the smooth thin shell instead of the base and directly secure the shell on top of the base. The top cover of the bottom shell was not only designed to protect the coil arrays but also to support the weight of the test subject. In this study, that weight would be the human's head or the phantom. The complete construction was printed with a 3D printer using Polycarbonate (PC). To fully and uniformly cover the shell, 24 coil arrays were divided into ten for the upper shell and fourteen for the bottom case. Both sides of the coil arrays were arranged in three rows in the craniocaudal direction.

To obtain a uniform image, the coils are designed to be similar in size and placed in bilateral symmetry. The coils were made primarily into circular loops, whereas some coils at the edge of the shell were formed into certain shapes to make the coverage area as large as possible. Fifteen coil arrays, including eight from the upper part shell and seven from the bottom case, were fashioned into circular loops of approximately 100-mm diameter. Six coil arrays were placed in a row at the edge of the bottom shell near the neck and were formed into an octagonal shape with an approximately 100-mm length between the furthest symmetrical edges. Two coil arrays at the position of the top of the eyes were fashioned into the shape of fish scales to cover both the eyes and nose, the distance between the peak and the top edge being 130 mm. In addition, one coil array at the top of the human's head was formed into a heart shape. All the coil arrays were formed manually from 14-AWG copper wires. The position for each coil is shown in Fig. 1, whereas the coil sizes are shown in Appendix A. Each loop contained four gaps to divide the loop into four equal parts, with each gap designed to accommodate a small printed circuit board (PCB). Each PCB had a different purpose, as shown in Fig. 2. The match and active-detune PCB comprised five components, capacitor C1 for matching to a resistance of 50 Ω, capacitor C2 and inductance L2 comprised an active detune circuit for image acquisition, inductance L1 was used for the radio frequency choke (RF-choke), and diode D1 is for switching the tune and detune status through the DC bias. The passive-detune PCB comprised three components, including a capacitor (C6), an inductance (L3), and a PIN diode (D2). The three components were constructed with consideration of safety issues. Capacitors C3, C4, and C5 were used to tune the circuit to the Lamour frequency and were placed separately at the opposite side. To minimize mutual coupling between the nearest coils, decoupling was achieved primarily by adjusting the overlapping area between the adjacent arrays (see Appendix B for overlapping area sizes). There was only one exception: the two coil arrays located at the top of the eye area were designed to share a single edge, and the decoupling between them was completed by adjusting the interconnecting capacitor. Low input impedance amplifiers (29 dB gain, 2.8 Ω for the input resistance, model number: PN2S10006, Suzhou Zhongzhi Medical Technology Co., Ltd) and preamplifier-decoupling (achieved by capacitor C7, C8) were also used to reduce the coupling between the next nearest coils. At last, in order to protect the circuit, inductors L4, L5, and L6 were used for RF-choke, while capacitors C9, C10, diode D3, and resistor R were used for protection circuit.

2.2. Coil testing on the bench

Bench testing was performed using a vector network analyzer (Agilent Technologies, E5061B) and a custom-made testing instrument that can offer independent control signals for each channel and 10 V for the preamplifiers. When the RF pulse was transmitted, the testing instrument would transfer a 100-mA current through the PIN diode on the active-detune board to detune the coil and would provide a -30 V voltage to keep the PIN diode inactive during image acquisition.

The bench measurement is referenced in [28]. For a single loop, both active-detune (comprised by capacitor C2 and inductance L2) and passive detune (L3 and C6) circuits were made to create short circuits for detuning during the transmitted RF pulse. To find the appropriate component values for detuning, the S_{21} parameter at the resonance frequency of the parallel LC circuit was measured by a probe of the vector network analyzers. The probe was connected in parallel with the inductance. Here, for the active-detune, the inductance L2 was 56 nH and the capacitor C2 was 39–61.6 pF, whereas these parameters were 27 or 68 nH for the inductance L3 and 27 or 20 pF for capacitor C6 at the passive-detune (see Appendix C for details on which component values were used for each coil array). The S_{21} parameter of the entire loop for estimating the tuning was also acquired afterwards by two decoupled (~70dB) inductive probe, with a distance of 2 cm between the coil and the probe. Moreover, coil matching was implemented to optimize noise performance after the preamplifier-board was connected

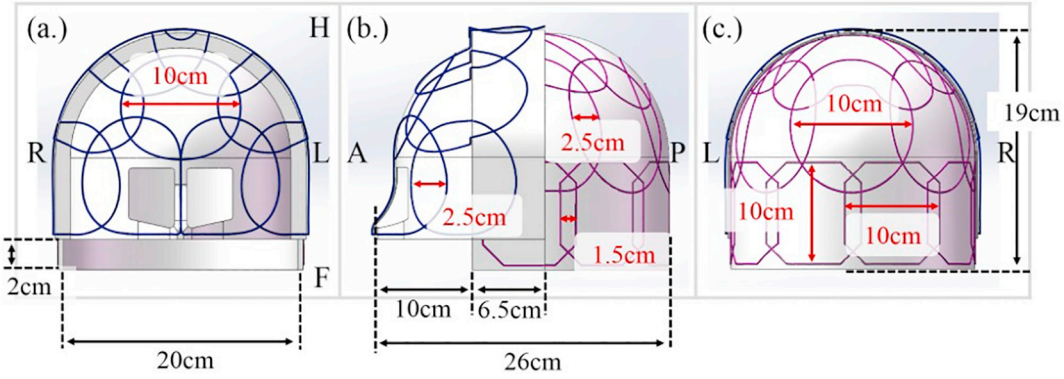

Fig. 1. The new head coil array: (a) top view, (b) side view, and (c) bottom view. The coverage area of the coil structure was designed to include a 20-cm ear-to-ear distance (width), 26-cm depth from noise to the back of the head, and 19 cm from the top of the head. The coil structure is large enough to fully cover the entire area of an adult human head. The region that covered the eyes was hollowed out to account for vision. The coil arrays were positioned at the inner side of the structure with the shell outside to protect them. The coils were primarily comprised of 10-cm-diameter circles and 10-cm-length squares.

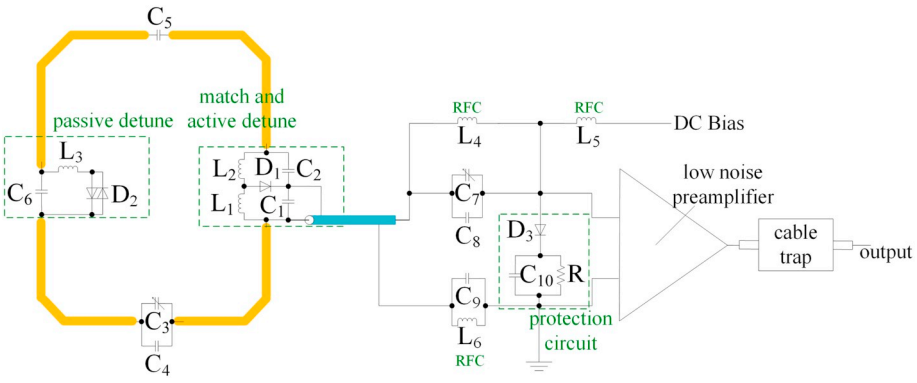

Fig. 2. The circuit diagram for all 24 coil arrays in the new head coil design. The inductance L2 and the capacitor C2 on the matched and active detune printed circle board (PCB) were constructed for detuning, whereas the inductance L3 and capacitor C6 at the passive detune PCB were used for safety. Capacitor C7 and C8 were used for preamplifier decoupling, and capacitor C9, C10, diode D4 and resistance R were designed for the protection circuit. In addition, the remaining capacitors were used for tuning and matching on the Larmor frequency, which will vary with each loop.

to the active-detune board with coaxial cable of about 42 to 99 mm in length. An S_{11} parameter on the log-mag format was performed by the vector network analyzers, with the pin-probe being placed in the header of the preamplifier-board. Notably, for good matching, the S_{11} value should be under −20 dB. To evaluate the active detuning performance, the S_{21} parameter was measured using the double-probe. The testing instrument transferred a bias current through the diode D1 to mimic the transmit state, and the detuning provided an isolation ($S_{21,detuned}$ -$S_{21,tuned}$) of the receive elements with average of −52 dB.

During the tuning and matching process, a Siemens commercial cylindrical phantom (filled with 1.24 g/L $NiSO_4{\cdot}6H_2O$ and 2.62 g/L NaCl, 160 mm in diameter, and 320 mm in length) was used to simulate the status of the human head. The loaded (Q_{unload}) and unloaded quality factors (Q_{unload}) were measured with and without the phantom.

For the coil array's decoupling, the overlapping adjacent coil elements method was employed. Generally, the isolations S_{21} between the adjacent and non-adjacent coils should be under −15 dB, which was measured when two loops were brought together with the other loops remaining in detuning mode.

2.3. Coil testing in the MRI

All the images studies were performed on the Siemens 3 T system (MAGNETOM Trio, a TIM system, Siemens Medical Solutions, Erlangen, Germany) and were compared with the Siemens 32-channel commercial head coil.

2.3.1. Phantom experiments

The Siemens Spherical Phantom (17 cm in diameter, filled with 1.24 g/L $NiSO_4{\cdot}6H_2O$ and 2.62 g/L NaCl) was used to simulate a human head on the SNR performance and the inverse geometry factor (g-factor) map studies. Two thin, green Siemens cushions were used to avoid any motion and ensure that the phantom remained at the center of both coils. A 2D gradient-recalled echo (GRE) sequence (TR/TE = 400 ms/10 ms, ETL = 39, ESP = 3.72 ms, slices per slab = 56, number of average = 2, iPAT = 2, spatial resolution = 0.69 × 0.7 × 0.7 mm^3, bandwidth = 751 Hz/pixel, and total scan time = 235 s) was used to acquire a central image of the phantom from three orientations. Noise images were also needed to calculate the SNR performance and analyze the noise correlation matrix, both of which were acquired from the same 2D GRE sequence with the transmitted voltage set to zero.

2.3.2. In vivo experiments

To evaluate the performance of the two coils in humans, five volunteers were scanned after approval of the study by our institutional review board (IRB). The scanning time for each volunteer was approximately 1 h. The same 2D GRE sequence used in the phantom study was also used in the *in vivo* study to evaluate SNR performance on the human brain. The slices were selected to acquire the images of the central brain area from the transverse, sagittal, and coronal orientations. Noise-only images were acquired with the same 2D GRE sequence by setting the transmit voltage to zero.

A 3D T1-weighted SPACE (Sampling Perfection with Application-Optimized Contrasts using different flip angle Evolution) sequence was used for the full brain structure imaging and the artery images, including the internal carotid artery (ICA), middle cerebral arteries (MCA), and basilar artery (BA). The 3D sequence had the following parameters: TR/TE = 861 ms/8.8 ms, slices per slab = 256, number of average = 1, iPAT = 2, spatial resolution = 0.5 × 0.5 × 0.5 mm^3, bandwidth = 579 Hz/pixel, echo spacing = 4.38 ms, and total scan time = 497 s.

2.4. Data analysis

The data analysis was based on the raw data and was completed using MATLAB (Mathworks, MA). Noise correlation matrices were calculated from noise images separately acquired using the following equation [25,29,30]:

$$\Psi_{mn} = \Delta x \Delta y \Delta z \times \sum_k \sigma_k (E_{km} E_{kn}^*) \qquad (m, n = 1, 2, ...24) \tag{1}$$

where ψ denotes the noise covariance matrix, E_{km} represents the local electric field of voxel k from channel m, σ_k is the local conductivity of voxel k, and Δx, Δy, *and* Δz are the voxel size in the x,y, and z directions (0.69, 0.7, and 0.7 mm, respectively).

The covariance weighted root-sum-of-squares (Cov-SoS) method was used to compute the SNR map on both the phantom and *in vivo* studies, and the following formula [31,32]:

$$\mathrm{SNR} = (S^H * \Psi^{-1} * S)^{\frac{1}{2}} \tag{2}$$

where S denotes the signal vector from the multichannel RF array and ψ represents the noise covariance matrix in the Eq. (1).

The acceleration ability evaluation is based on the g-factor calculation in the phantom study. Full-sampled data were required, followed by down-sampling along the phase-encoding direction by using the sensitivity encoding (SENSE) method [32,33]. The phase-encoding direction was selected as right-to-left in the transverse orientation, anterior-to-posterior in the sagittal orientation, and head-to-foot in the coronal orientation. The corresponding g-factor map was found using the following formula:

$$g_p = \sqrt{\left[\frac{1}{SNR^2}\right]_{pp} * [SNR^2]_{pp}} \tag{3}$$

where g_p denotes the g-factor corresponding to the pixel p.

3. Results

3.1. Coil testing on the bench

The average Q_{ratio} (Q_{unload}/Q_{load}) for the new head coil array was

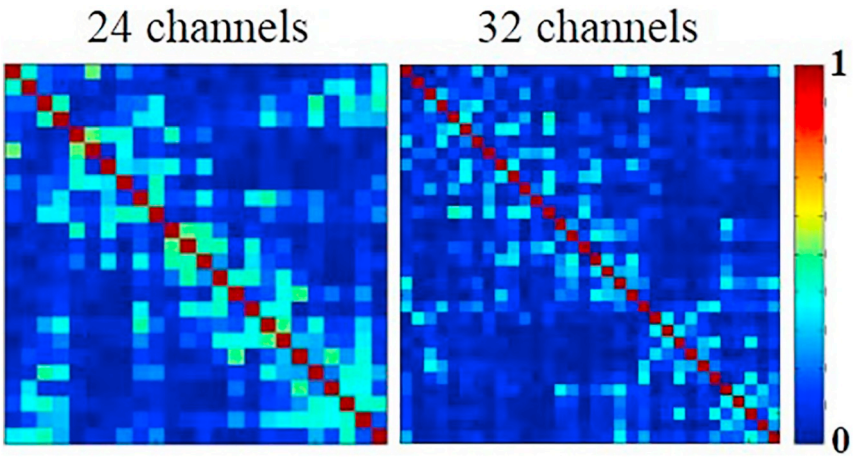

Fig. 3. The noise correlations of the 24-channel new head coil array (left side) and the 32-channel Siemens commercial head coil array (right side) generated from acquisition without RF excitation. The maximum value of the noise correlation from the new head coil is 0.51 and 0.37 for the commercial head coil, whereas the mean value of the correlation between two random coil arrays is 0.23 for new head coil and 0.08 for the commercial head coil.

~73/47. The active detune was adjusted to under −67 dB. The preamplifier decoupling was adjusted to under −49 dB, whereas the preamplifier was given a −30 V voltage. The decoupling value between two neighboring elements (S_{12}) was −17.5 dB, on average.

3.2. Coil testing on MRI

Fig. 3 shows the noise correlation matrices of the new head coil array and the commercial head coil array. The values of the matrices were calculated using only the elements from the off-diagonal. The values were 0.23 and 0.51, respectively, for the mean and maximum in the new head coil and 0.08 and 0.37, respectively, for the commercial head coil array.

3.3. Phantom experiments

The SNR maps of the new head coil array and commercial head coil array are shown in Fig. 4 (a.) and (b.), respectively. The slices pass through the center of the phantom in each orientation. The mean value of the entire phantom graphic was calculated under the related image. Fig. 4 (c.) shows the ratio of Fig. 4 (a.) and (b.), specifically, 110%, 113%, and 102%, in the transverse, sagittal, and coronal slices, respectively.

The inverse g-factor images are displayed in Fig. 5. The images were scanned through the center of the phantom in three orientations. The mean and maximum values of the g-factor were calculated under the full region of the phantom and are noted under the images as $mean_{g\text{-}factor}/max_{g\text{-}factor}$. From Fig. 5, the $mean_g$-factor had under a 1% difference between both coils in the transverse and sagittal orientations, but the difference rose among the acceleration on the coronal orientation to 12.8%.

3.4. In vivo experiments

Fig. 6 shows the SNR measurement results and related images of a human in the 2D GRE sequence. The blue-color background shows the SNR maps calculated from the black-color background images. A central line was used to analyze the SNR performance in red for the new head coil and blue for the commercial head coil for each orientation. The brain zone is marked on the SNR graph, with the mean value calculated beneath the graph. The difference in the mean value was calculated using the following equation: $[(SNR_{commercial} - SNR_{new}) / SNR_{commercial}] \times 100$, pixel by pixel in the brain zone, and the percentile was under 8% in all three orientations. The same SNR measurement experiment was tested successfully in four other humans, verifying the reproducibility of the results.

The 3D T1-weighted SPACE image was used for the artery images. The arterial system from the M1 segment of ICA to the M2 segment of MCA is displayed in Fig. 7 in the coronal orientation, with three cross-sectional view of the arteries. ① Shows the M1 segment of MCA; ② shows the C7 segment Communicating segment) of ICA; and ③ shows the C2 segment (Petrous segment) of the ICA. Fig. 8 shows the BA images in the sagittal orientation, with the coronal orientation at the top solid insets, and cross sectional view at the bottom dashed insets.

4. Discussion

In this study, a new 24-channel head coil array was presented for imaging of the human brain, as well as the intracranial vessel wall. The new head coil showed comparable SNR performance with the commercial 32-channel head coil and had adequate g-factors for the acceleration factors from 2 to 4 during the phantom study. The *in vivo* study showed a consistent SNR in several human studies and provided high image quality in the 3D brain structure and artery images.

The proposed head coil array has fewer coil elements or channels compared with the 32-channel commercial head coil, providing more design flexibility in selection of size, geometry and layout of array elements to meet the needs of specific imaging applications. With less channel counts, it simplifies the design and reduces the challenges in achieving sufficient electromagnetic decoupling among the resonant elements. Given the less number of electric components and subsystem used, Strategies using less channel counts also reduce the costs of coil arrays and increase the reliability and robustness of operation.

Although the new head coil reduced the difficulty of the process and its financial burden, the coil performance still approximated that of the commercial head coil. In the phantom study, the new head coil had a similar SNR distribution as the commercial head coil, particularly near the center of the phantom. This is because the new head coil has a larger coil array size that can accommodate the inner part of the object with less attenuation while passing the signal [9]. The acceleration ability of the new head coil was as good as that of the commercial head coil during the acceleration direction from right-to-left and anterior-to-posterior, under an acceleration factor of 4. Moreover, the new head coil had a slightly better acceleration ability in these two directions when the acceleration factor reached 4. However, the new head coil demonstrated unsatisfactory acceleration compared with the commercial head coil in the head-to-foot acceleration direction. This is because the lower the array count in the acceleration direction, the worse the

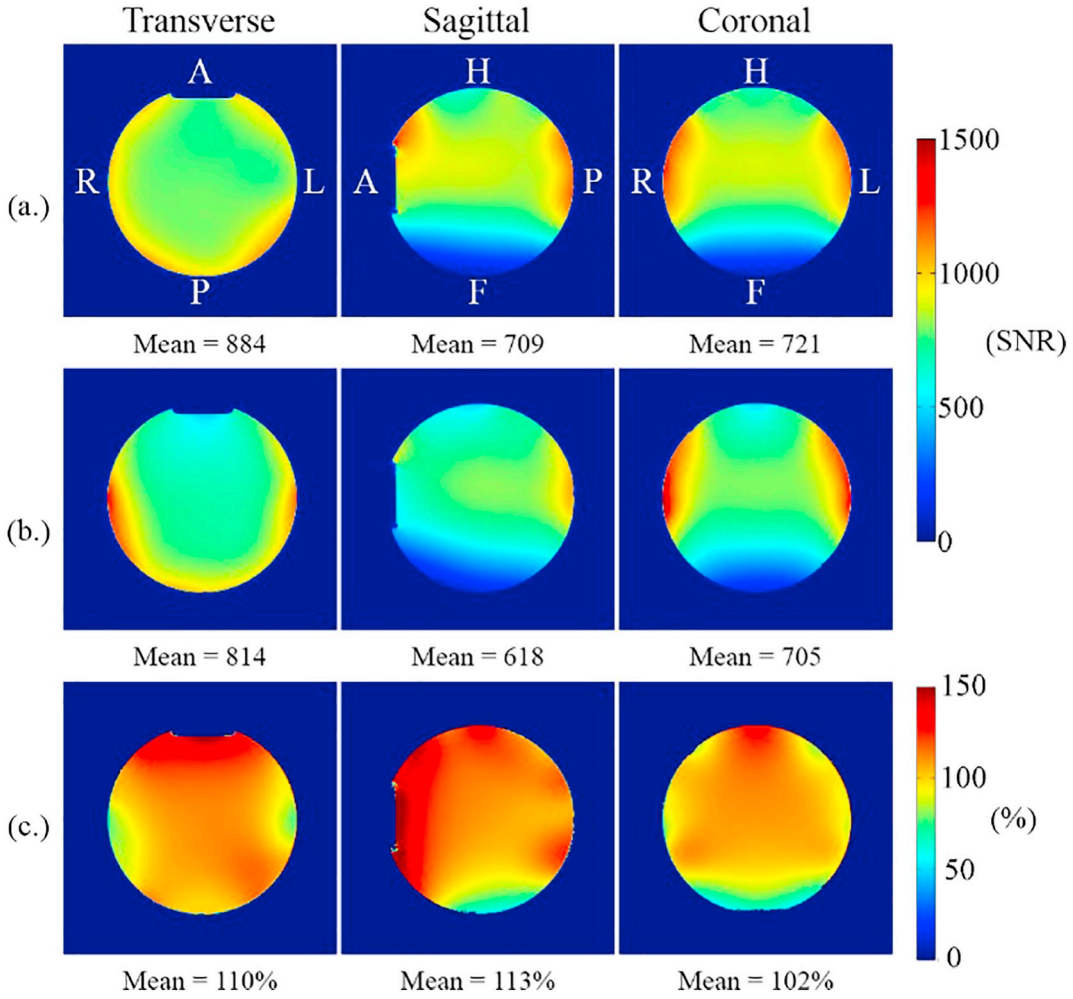

Fig. 4. The signal-to-noise ratio map (SNR map) from the 24-channel new head coil array (a.) and the 32-channel commercial head coil array (b.) are shown in the first two rows of the figure. The orientations were selected to cut through the phantom's central direction and place it in the transverse, sagittal, and coronal directions from left-to-right in the figure. The bottom row (c.) is the ratio calculated by (a.)/(b.) × 100%, pixel by pixel. The 2D GRE sequence was used with the following parameters: TR = 300 ms, TE = 10 ms, bandwidth = 130 Hz/pixel, FOV = 250 × 250 mm^2, slice thickness = 3 mm, acquisition matrix = 256 × 256, flip angle = 60°, slice number = 1, and measurement = 1.

acceleration capability. The commercial head coil has one more row coil elements than the new head coil in coronal orientation, so new head coil has a lower acceleration capability in this direction. In the coronal orientation, the two head coils had a closer performance with a low acceleration factor, less than 1% when the acceleration factor was 2. The gap grew rapidly when the factor rose, expanding to 12.8% when the acceleration factor was 4.

In the *in vivo* study, the performance of the SNR maps of the 2D sequences matched the results of the phantom study. This shows that the new head coil had a similar capacity to the commercial head coil for scanning the 2D structural image in humans. By adjusting the brain structure and intracranial vessel wall images to the same scale, the images both coils displayed were very similar. For brain structure and intracranial vessel wall researchers, the new head coil offers an additional option, with fewer challenges in building the coil, a lower price, and obtaining close structural images on 2D and 3D sequences.

Although the new head coil has multiple advantages, it also has limitations. The coil number cutoff not only decreases the difficulty of building the coil but also reduces the acceleration capability; in this work, the acceleration capability of the head-to-foot direction was sacrificed. A larger coil size affirmed the SNR from the center of the brain, but this design is not an optimal option for the SNR around the edges. In both the phantom and *in vivo* studies, the new head coil had a lower SNR than the commercial head coil at the edges. According to the noise-correlation results compare with the commercial head coil, there is potential to improve in decoupling, which leads to the possibility of gain in the SNR performance.

Given the previously described details, we believe that our coil has comparable SNR performance with the commercial 32-channel head coil in both the phantom and *in vivo* studies and adequate acceleration performance in the anterior-to-posterior and right-to-left directions with an acceleration factor from 2 to 4, which is the most often used acceleration direction for vessel wall images. It also offers high image quality for 3D brain structure and artery images. All the features demonstrate that the new head coil is an appropriate design for head imaging, particularly for artery and vessel wall images.

5. Conclusions

We presented a new head coil as an additional option for brain MR imaging. This new coil design with less channel counts reduces the challenge and cost of building the device but provides comparable

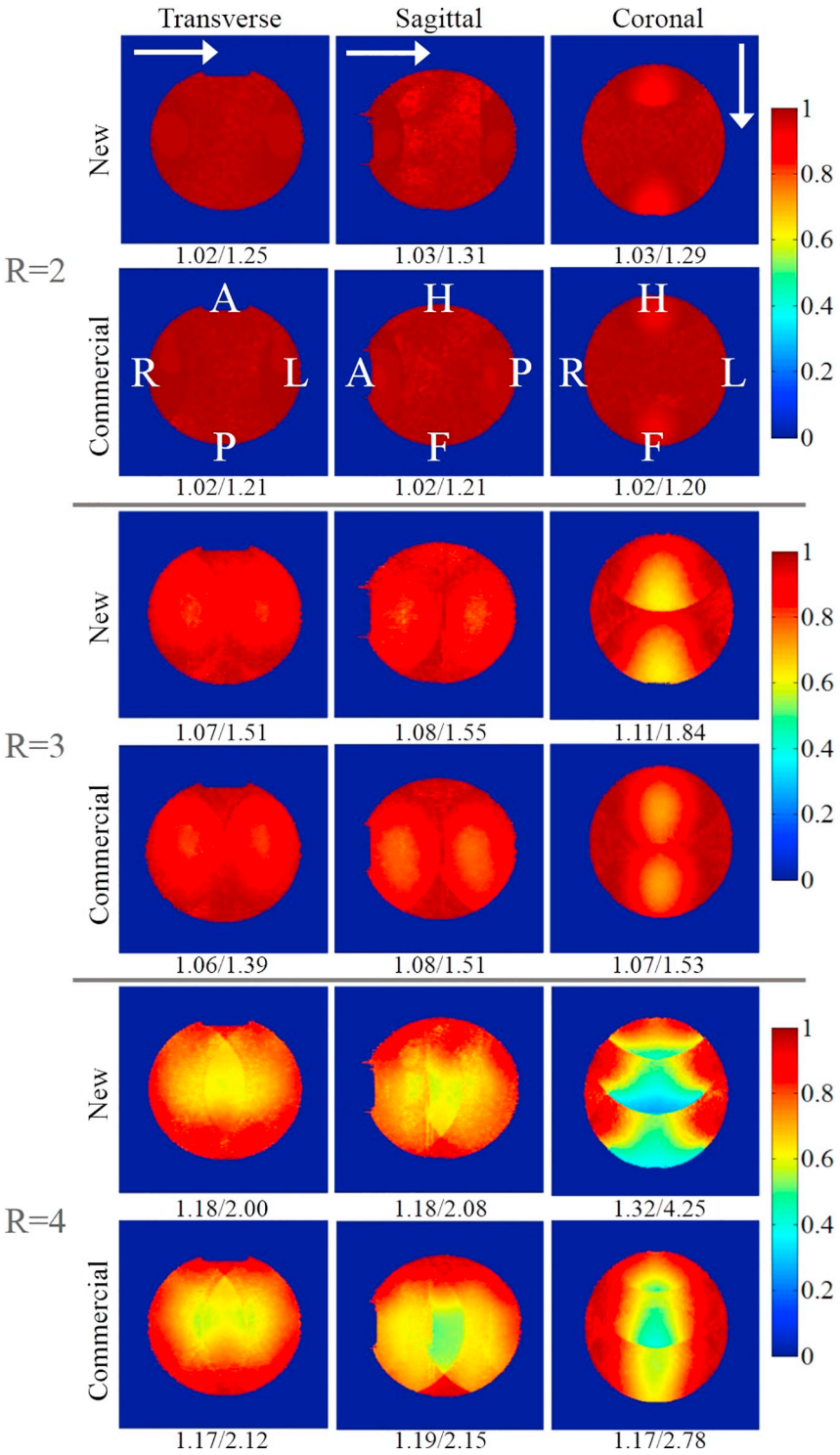

Fig. 5. The inverse g-factor images of the new head coil array and commercial head coil array with acceleration rates of 2, 3, and 4. The acceleration directions are shown as the white-color arrow. The g-factor values of the mean and maximum are displayed under each related inverse g-factor image. The mean values are on the left and the maximum values are on the right. The 2D GRE sequence was used with the following parameters: TR = 300 ms, TE = 10 ms, bandwidth = 130 Hz/pixel, FOV = 250 × 250 mm^2, slice thickness = 3 mm, acquisition matrix = 256 × 256, flip angle = 60°, slice number = 1, and measurement = 1.

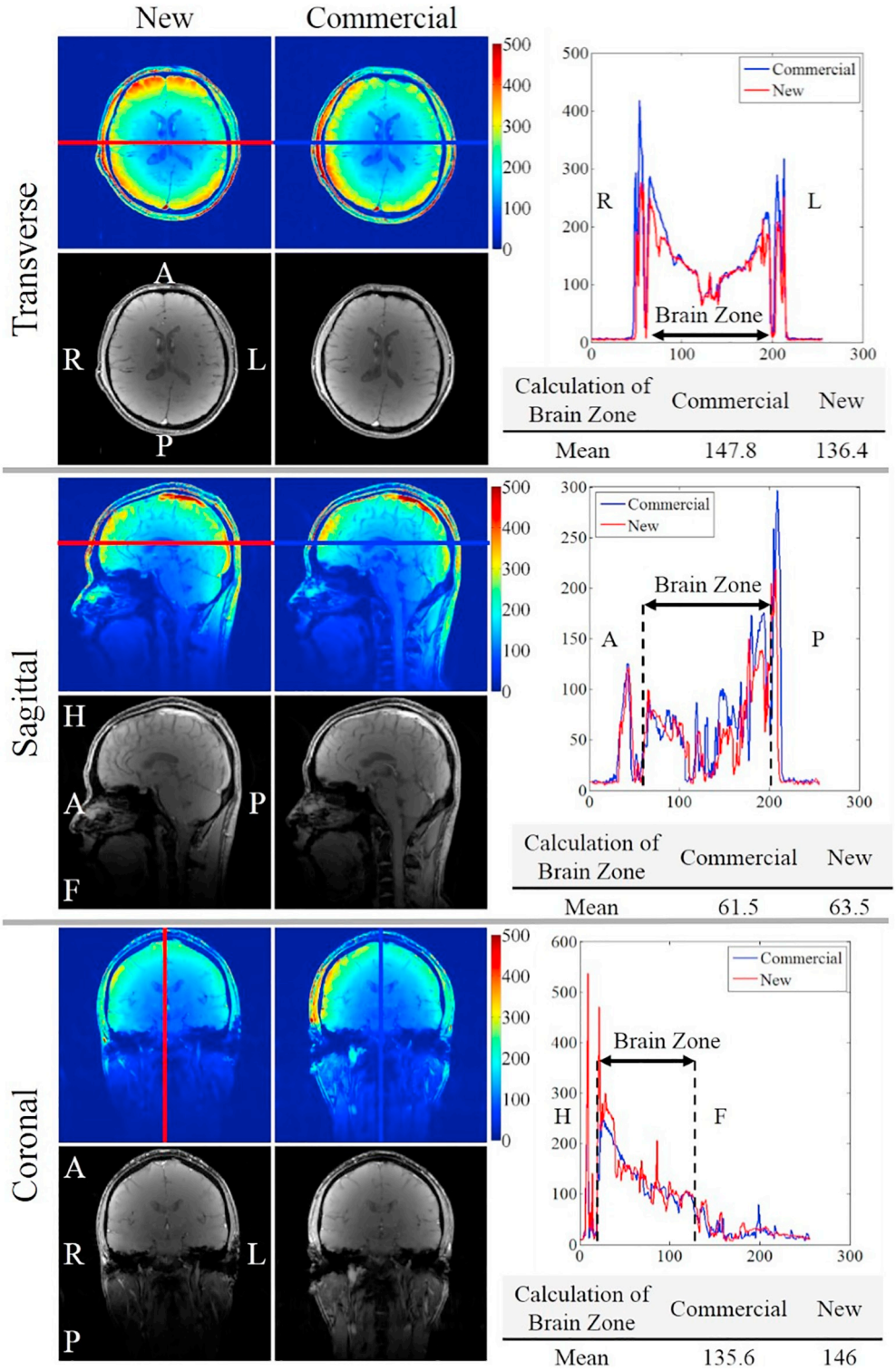

Fig. 6. The SNR maps (color images) and the related image (grayscale images) from the new head coil and commercial head coil from the same participant. The SNR profiles (blue line for the commercial head coil and red line for the new head coil) were selected to pass through the center of the brain in different directions with each orientation. (For interpretation of the references to color in this figure legend, the reader is referred to the web version of this article.)

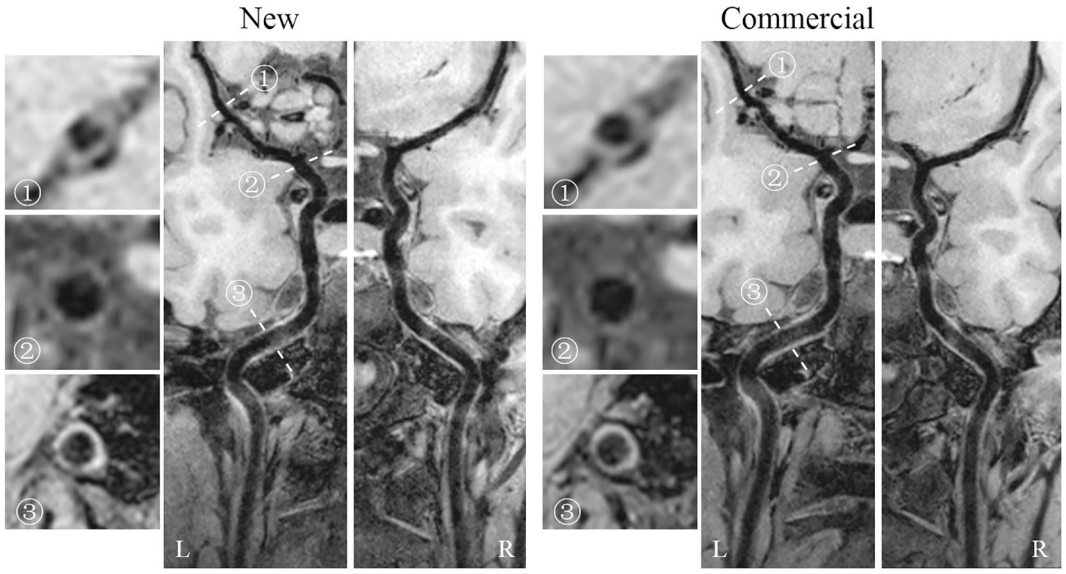

Fig. 7. Both the right and left sides of the arterial system from the M1 segment of ICA to the M2 segment of MCA are shown in the curved multiplanar reconstruction images from the 3D T1-weighted sequence. The case demonstrated the ability of both coil arrays to delineate arterial walls at different arterial segments. The cross sectional view of the arteries at three different locations are shown. ① Shows the M1 segment of MCA; ② shows the C7 segment Communicating segment) of the ICA; and ③ shows the C2 segment (Petrous segment) of the ICA.

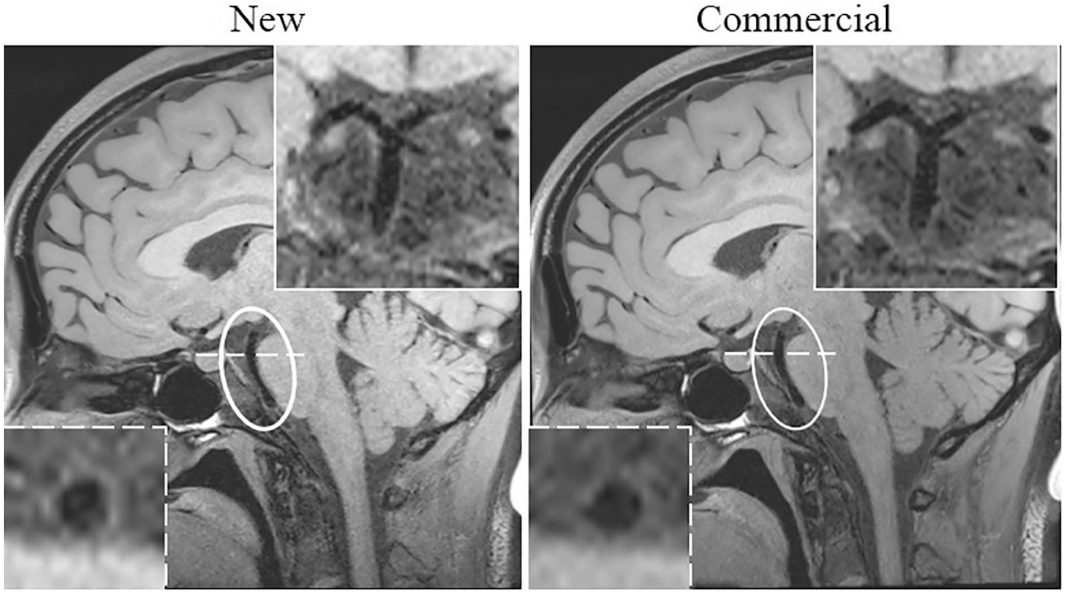

Fig. 8. The basilar artery (BA) images from the 3D T1-weighted sequence (TR/TE = 861 ms/8.8 ms, slices per slab = 256, number of averages = 1, iPAT = 2, spatial resolution = 0.5 × 0.5 × 0.5 mm^3, bandwidth = 579 Hz/ pixel, echo spacing = 4.38 ms, and total scan time = 497 s). The images were fused to match the same section and have the same color scaling. The top solid insets show the coronal orientation from the main images, whereas the bottom dashed insets show the cross-sectional view of the arteries.

imaging capability to the commercial head coil with higher channel counts, in the aspects of SNR performance, brain structural imaging, and intracranial arterial wall imaging at 3 Tesla. With less electronic components, resonant elements and subsystems, the coil array using the less channel count strategy is expected to be more reliable and robust in practice. Additionally, when the RF channel number of MR scanners is fixed and limited, it may become possible and convenient to combine this low channel count head coil array with other coils for some applications, *e.g.*, combination of the head coil and neck coil for stroke imaging.

Acknowledgements

This work was supported in part by NSFC under Grant No. 61571433, 81527901, 81527901, 81327801, 81571669, 81627901, and 81801691; Guangdong Province grants 2014A030313691, 2015B020214006, and 2014B030301013; Youth Innovation Promotion Association of CAS No. 2017415; city grants KQJSCX20160301143250, KQCX2015033117354154, and JCYJ20170413161314734; and a Pengcheng Scholar Award.

Appendix A

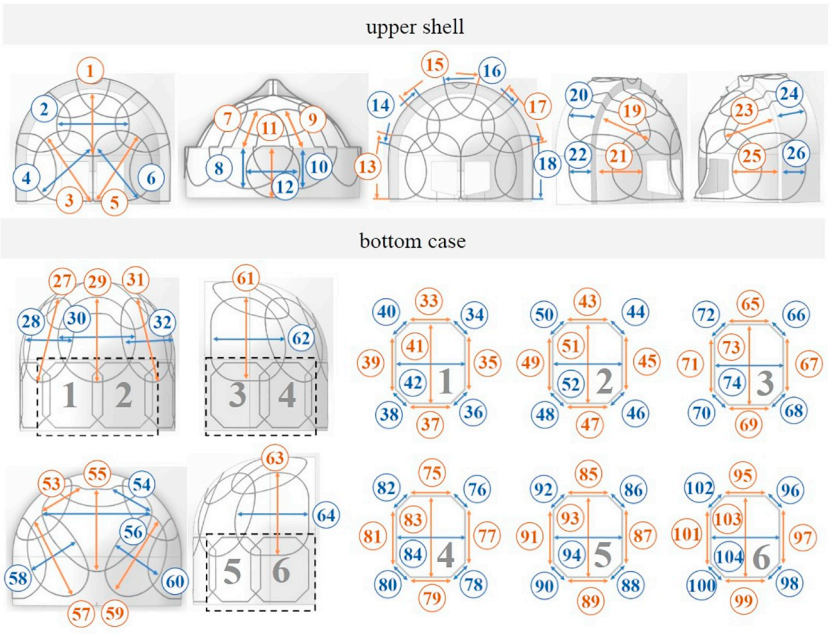

(1) - (10)	110	105	130	105	130	105	40	55	39	56
(11) - (20)	110	108	103	95	103	100	85	85	70	56
(21) - (30)	50	35	70	56	48	35	90	85	90	85
(31) - (40)	80	80	40	30	75	20	50	20	75	20
(41) - (50)	100	85	40	20	70	20	50	20	70	40
(51) - (60)	100	85	55	60	95	100	110	90	105	90
(61) - (70)	90	95	90	100	50	20	70	20	55	20
(71) - (80)	70	20	100	85	50	15	70	20	55	20
(81) - (90)	75	20	100	85	20	55	70	20	60	20
(91) - (100)	75	20	100	85	45	20	65	20	55	15
(101) - (104)	80	30	100	85	length unit: mm					

Fig. A. Coil dimensions of each coil elements.

Appendix B

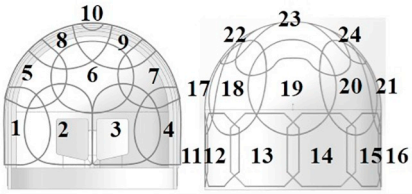

model number

fixed capacitor (C1,C2,C4,C5,C6,C7):
100B series, ATC(written in black);
70B series, Dalicap(written in red);
inductance(L2,L3):1812SMS series, Coilcraft ;
coaxial cable: V4566-B11-G7, LEONI;

coil number	1	2	3	4	5	6	7	8	9	10
C1(pF)	56//5.6	43	43	56//5.6	56	47	56	10//56	10//56	27//56
L1 (uH)	2.7uH (1008CS-272XJLD, Coilcraft)									
C2(pF)	39	39	39	3.9//39	39	39	4.7//56	39	39	39
L2(nH)	56									
D1	DH80055-40N, temex									
C3(pF)	JR400, VOLTRONICS									
C4(pF)	15	10	10	12	10	15	12	15	15	15
C5(pF)	10	24 // JR400		20	20	22	10	22	22	27
C6(pF)	20	20	20	20	20	27	20	27	27	27
L3(nH)	68	68	68	68	68	27	68	27	27	27
D2	UMX9989AP, MICROSEMI									
L4,L5,L6 (uH)	2.7uH (1008CS-272XJLD, Coilcraft)									
C7(pF)	22									
C8(pF)	JR400, VOLTRONICS									
C9,C10(nF)	1nF (1206, Syfer Technology Limited)									
D3	BA592, Infineon Technologies									
R(ohms)	27 ohms (CMF-N0805, microtech GmbH electronic)									
C-Cable (mm)	52	46	45	61	77	67	72	47	55	47

coil number	11	12	13	14	15	16	17	18	19	20	21	22	23	24
C1(pF)	4.7//39	56//10	15//56	15//56	18//56	4.7//36	56	56	56	4.7//56	56	56	47	56
L1(uH)	2.7uH (1008CS-272XJLD, Coilcraft)													
C2(pF)	56//5.6	39	49	43	43	56//5.6	39//4.7	2.7//39	39	39	39	4.7//39	39	39
L2(nH)	56													
D1	DH80055-40N, temex													
C3(pF)	JR400, VOLTRONICS													
C4(pF)	15	15	15	18	15	15	15	20	20	20	15	15	12	12
C5(pF)	22	22	22	18	22	22	27	27	27	27	27	27	27	27
C6(pF)	27													
L3(nH)	27													
D2	UMX9989AP, MICROSEMI													
L4,L5,L6 (uH)	2.7uH (1008CS-272XJLD, Coilcraft)													
C7(pF)	22													
C8(pF)	JR400, VOLTRONICS													
C9,C10(nF)	1nF (1206, Syfer Technology Limited)													
D3	BA592, Infineon Technologies													
R(ohms)	27 ohms (CMF-N0805, microtech GmbH electronic)													
C-Cable (mm)	68	58	42	49	49	70	61	71	54	72	65	99	98	89

C-Cable: coaxial cable length

Fig. B. The long, short axis and area size of each overlap area.

Appendix C

upper shell

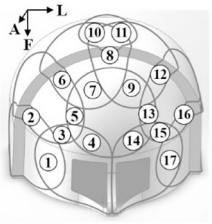

numbering	①	②	③	④	⑤	⑥	⑦	⑧	⑨
overlap area (mm^2)	1300	1400	1400	900	100	1500	1200	1300	1200
long axis (mm)	70	80	70	65	70	70	60	90	55
short axis (mm)	35	30	25	30	23	30	27	25	30

numbering	⑩	⑪	⑫	⑬	⑭	⑮	⑯	⑰
overlap area (mm^2)	1100	1100	1400	1000	900	1100	1300	1000
long axis (mm)	70	75	80	70	65	75	90	70
short axis (mm)	20	20	23	24	27	25	30	25

bottom case

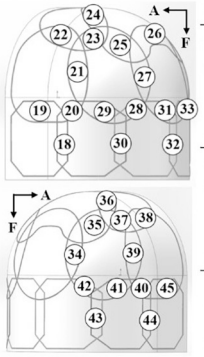

numbering	⑱	⑲	⑳	㉑	㉒	㉓	㉔	㉕	㉖	㉗
overlap area (mm^2)	900	900	1200	1000	900	1000	1400	800	1400	900
long axis (mm)	85	65	60	65	65	65	95	55	85	65
short axis (mm)	15	25	25	25	16	20	25	25	20	25

numbering	㉘	㉙	㉚	㉛	㉜	㉝	㉞	㉟	㊱	㊲
overlap area (mm^2)	1200	1200	900	1100	900	1100	800	800	1400	800
long axis (mm)	60	55	85	60	85	60	60	50	90	55
short axis (mm)	20	25	14	18	15	18	20	25	25	20

numbering	㊳	㊴	㊵	㊶	㊷	㊸	㊹	㊺
overlap area (mm^2)	1100	800	900	900	1100	900	900	1100
long axis (mm)	75	65	50	60	55	85	85	75
short axis (mm)	25	20	20	18	15	15	15	25

combined

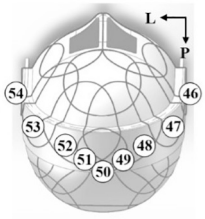

numbering	㊻	㊼	㊽	㊾	㊿	(51)	(52)	(53)	(54)
overlap area (mm^2)	2300	800	700	600	1500	600	700	800	2300
long axis (mm)	95	45	35	40	70	45	35	45	95
short axis (mm)	25	35	25	25	30	25	25	35	25

Fig. C. The value, model number, and manufacturers of all the components that were used. The two schematic diagrams at the top of the figure show the coil number and position of each coil array.

References

[1] Balu N, Yarnykh VL, Scholnick J, Chu B, Yuan C, Hayes C. Improvements in carotid plaque imaging using a new eight-element phased array coil at 3T. J Magn Reson Imaging 2009;30(5):1209–14.

[2] Cohen-Adad J, Mareyam A, Keil B, Polimeni JR, Wald LL. 32-channel RF coil optimized for brain and cervical spinal cord at 3 T. Magn Reson Med 2011;66(4):1198–208.

[3] van der Kolk AG, Hendrikse J, Brundel M, Biessels GJ, Smit EJ, Visser F, et al. Multi-sequence whole-brain intracranial vessel wall imaging at 7.0 tesla. Eur Radiol 2013;23(11):2996–3004.

[4] Xie Y, Yang Q, Xie G, Pang J, Fan Z, Li D. Improved black-blood imaging using DANTE-SPACE for simultaneous carotid and intracranial vessel wall evaluation. Magn Reson Med 2016;75(6):2286–94.

[5] Zhang X, Ugurbil K, Chen W. Microstrip RF surface coil design for extremely high-field MRI and spectroscopy. Magn Reson Med 2001;46(3):443–50.

[6] Zhang X, Ugurbil K, Chen W. A microstrip transmission line volume coil for human head MR imaging at 4T. J Magn Reson 2003;161(2):242–51.

[7] Porter JR, Wright SM, Reykowski A. A 16-element phased-array head coil. Magn Reson Med 1998;40(2):272–9.

[8] Roemer PB, Edelstein WA, Hayes CE, Souza SP, Mueller OM. The NMR phased array. Magn Reson Med 1990;16(2):192–225.

[9] Wright SM, Wald LL. Theory and application of array coils in MR spectroscopy. NMR Biomed 1997;10(8):394–410.

[10] Xin X, Han J, Feng Y, Feng Q, Chen W. Inverse design of an organ-oriented RF coil for open, vertical-field, MR-guided, focused ultrasound surgery. Magn Reson Imaging 2012;30(10):1519–26.

[11] Adriany G, Van de Moortele PF, Wiesinger F, Moeller S, Strupp JP, Andersen P, et al. Transmit and receive transmission line arrays for 7 Tesla parallel imaging. Magn Reson Med 2005;53(2):434–45.

[12] Li Y, Zhang X. Advanced MR imaging Technologies in Fetuses. OMICS J Radiol 2012;1(4):e113.

[13] Reiss-Zimmermann M, Gutberlet M, Kostler H, Fritzsch D, Hoffmann KT. Improvement of SNR and acquisition acceleration using a 32-channel head coil compared to a 12-channel head coil at 3T. Acta Radiol 2013;54(6):702–8.

[14] Schmitt M, Potthast A, Sosnovik DE, Polimeni JR, Wiggins GC, Triantafyllou C, et al. A 128-channel receive-only cardiac coil for highly accelerated cardiac MRI at 3 Tesla. Magn Reson Med 2008;59(6):1431–9.

[15] Wintersperger BJ, Reeder SB, Nikolaou K, Dietrich O, Huber A, Greiser A, et al. Cardiac CINE MR imaging with a 32-channel cardiac coil and parallel imaging: impact of acceleration factors on image quality and volumetric accuracy. J Magn Reson Imaging 2006;23(2):222–7.

[16] Wu B, Li Y, Wang C, Vigneron DB, Zhang X. Multi-reception strategy with improved SNR for multichannel MR imaging. PLoS One 2012;7(8):e42237.

[17] Wu B, Zhang X, Wang C, Li Y, Pang Y, Lu J, et al. Flexible transceiver array for ultrahigh field human MR imaging. Magn Reson Med 2012;68(4):1332–8.

[18] Pruessmann KP. Encoding and reconstruction in parallel MRI. NMR Biomed 2006;19(3):288–99.

[19] Connell IR, Gilbert KM, Abou-Khousa MA, Menon RS. MRI RF array decoupling method with magnetic wall distributed filters. IEEE Trans Med Imaging 2015;34(4):825–35.

[20] Georget E, Luong M, Vignaud A, Giacomini E, Chazel E, Ferrand G, et al. Stacked magnetic resonators for MRI RF coils decoupling. J Magn Reson 2017;275:11–8.

[21] Lattanzi R, Wiggins GC, Zhang B, Duan Q, Brown R, Sodickson DK. Approaching ultimate intrinsic signal-to-noise ratio with loop and dipole antennas. Magn Reson Med 2018;79(3):1789–803.

[22] Li Y, Xie Z, Pang Y, Vigneron D, Zhang X. ICE decoupling technique for RF coil array designs. Med Phys 2011;38(7):4086–93.

[23] Pang Y, Wu B, Jiang X, Vigneron DB, Zhang X. Tilted microstrip phased arrays with improved electromagnetic decoupling for ultrahigh-field magnetic resonance imaging. Medicine (Baltimore) 2014;93(28):e311.

[24] Pang Y, Wu B, Wang C, Vigneron DB, Zhang X. Numerical analysis of human sample effect on RF penetration and liver MR imaging at ultrahigh field. Concepts Magn

Reson Part B: Magn Reson Eng 2011;39B(4):206–16.
[25] Yan X, Cao Z, Zhang X. Simulation verification of SNR and parallel imaging improvements by ICE-decoupled loop array in MRI. Appl Magn Reson 2016;47(4):395–403.
[26] Yan X, Xie Z, Pedersen JO, Zhang X. Theoretical analysis of magnetic wall decoupling method for radiative antenna arrays in ultrahigh magnetic field MRI. Concepts Magn Reson Part B: Magn Reson Eng 2015;45(4):183–90.
[27] Yan X, Xue R, Zhang X. Closely-spaced double-row microstrip RF arrays for parallel MR imaging at ultrahigh fields. Appl Magn Reson 2015;46(11):1239–48.
[28] Fujita H, Zheng T, Yang X, Finnerty MJ, Handa S. RF surface receive array coils: the art of an LC circuit. J Magn Reson Imaging 2013;38(1):12–25.
[29] Cao Z, Oh S, Sica CT, McGarrity JM, Horan T, Luo W, et al. Bloch-based MRI system simulator considering realistic electromagnetic fields for calculation of signal, noise, and specific absorption rate. Magn Reson Med 2014;72(1):237–47.
[30] Ocali O, Atalar E. Ultimate intrinsic signal-to-noise ratio in MRI. Magn Reson Med 1998;39(3):462–73.
[31] Keil B, Wald LL. Massively parallel MRI detector arrays. J Magn Reson 2013;229:75–89.
[32] Pruessmann KP, Weiger M, Scheidegger MB, Boesiger P. SENSE: sensitivity encoding for fast MRI. Magn Reson Med 1999;42(5):952–62.
[33] Ying L, Liang ZP. Parallel MRI using phased array coils. IEEE Signal Process Mag 2010;27(4):90–8.